

Reflectance calibration and shadow effect of VNIS spectra acquired by the Yutu rover

Sen Hu¹, Yang-Ting Lin¹, Bin Liu², Wei Yang¹, Zhi-Ping He³ and Wei-Fan Xing^{1,4}

¹ Key Laboratory of Earth and Planetary Physics, Institute of Geology and Geophysics, Chinese Academy of Sciences, Beijing 100029, China; linyut@mail.iggcas.ac.cn

² Key Laboratory of Lunar and Deep Space Exploration, National Astronomical Observatories, Chinese Academy of Sciences, Beijing 100012, China

³ Key Laboratory of Space Active Opto-Electronics Technology, Shanghai Institute of Technical Physics, Chinese Academy of Sciences, Shanghai 200083, China

⁴ China University of Geosciences, Wuhan 430074, China

Received 2014 September 10; accepted 2015 March 13

Abstract Yutu is the first lunar rover after the Apollo program and Luna missions. One of the payloads on the Yutu rover, the Visible and Near-infrared Imaging Spectrometer (VNIS), has acquired four VIS/NIR images and SWIR spectra near its landing site in Mare Imbrium. The radiance images were reduced through repairing bad lines and bad points, and applying flat field correction, and then were converted into reflectance values based on the solar irradiance and angles of incidence. A significant shadow effect was observed in the VIS/NIR image. The shadowed regions show lower reflectance with a darkening trend compared with illuminated regions. The reflectance increased by up to 24% for entire images and 17% for the VIS/NIR-SWIR overlapping regions after shadow correction. The correction for the shadow effect will remarkably decrease the estimate of FeO content, by up to 4.9 wt.% in this study. The derived FeO contents of CD-005~008 after shadow correction are around 18.0 wt.%.

Key words: Moon — Chang'e-3 — Yutu — VNIS — shadow — reflectance

1 INTRODUCTION

The major scientific objective of Chang'e-3 was to provide new constraints on the formation and evolution history of the Moon via in-situ use of its Alpha Particle-induced X-ray Spectrometer (APXS), Visible and Near-infrared Imaging Spectrometer (VNIS), terrain camera and Lunar Penetrating Radar (LPR) in analyses of lunar rocks and soils. On 2013 December 14, Chang'e-3 successfully soft landed in the northern part of Mare Imbrium. The TiO₂ contents acquired by Clementine UV-VIS data, SELENE MI data and Chang'e-1 Interference Imaging Spectrometer (IIM) data indicate multiple volcanic lava flows occurred beneath the landing site (Gillis et al. 2003; Ohtake et al. 2012; Wu et al. 2012). In addition, the age of volcanism determined by crater chronology is 1–2.5 Ga (Shultz & Spudis 1983), indicating there has been young volcanic activity on the Moon. The in-situ detections by Chang'e-3 around the landing site will supply new constraints to study examples of young geologic activity on the Moon.

The VNIS can acquire images in the range of 450–945 nm (VIS/NIR) and spectra in the range of 900–2395 nm (SWIR) (He et al. 2011; Liu et al. 2013; He et al. 2014a,b; Liu et al. 2014). The visible to near infrared spectrum of the Moon is closely correlated with chemical compositions (Lucey et al. 2000) and physical properties (Helfenstein & Shepard 1999; Shkuratov et al. 2011). The Level 2B data from VNIS, published by the Ground Segment for Data, Science and Application (GSDSA) of China's Lunar Exploration Program, were reduced and converted to calibrated reflectance, based on the processing of raw data (salt and pepper noise subtraction, dark current subtraction and non-uniformity correction) (Liu et al. 2014). Unlike detections made from orbit, the in-situ analyses on the lunar surface are constrained by the observation angles and surface roughness, which cause significant shadow effects. Therefore, in this work, we briefly introduce the VNIS data (Sect. 2) and reflectance calibration method (Sect. 3) at first, then focus on the shadow effect (Sect. 4) of the in-situ VNIS spectra, and finally assess the impact of the shadow effect on chemical composition inversion (Sect. 5).

2 VNIS DATA AND PROCESSING

The VNIS data on the Yutu rover were published in PDS format. The Level 2B data were used in this work. The header file of the data recorded the solar angle of incidence, rover geographic location, integration time and some other observation information, which were used for reflectance calibration. Four local regions were measured by the Yutu rover in the first two lunar days and were designated as CD-005~008 (Table 1). The VIS/NIR (450–945 nm) data were recorded as images with 256×256 pixels. The spatial resolution is around 0.5 mm and the spectral interval is 5 nm. The SWIR (900–2395 nm) data were recorded as spectra with a spectral interval of 5 nm (He et al. 2014a).

Table 1 Information about Level 2B Data Used in this Work

File name	Designation	i^a	Distance ^b	Integration time
CE3-**-0005-A.2B	CD-005	59.884967	(-0.22, -19.79)	VIS: 40 min, NIR: 32 min
CE3-**-0006-A.2B	CD-006	67.486938	(-0.66, -32.05)	VIS: 18 min, NIR: 8 min
CE3-**-0007-A.2B	CD-007	69.721666	(-13.30, -36.36)	VIS: 31 min, NIR: 32 min
CE3-**-0008-A.2B	CD-008	54.065078	(-24.65, -32.63)	VIS: 40 min, NIR: 32 min

Notes: ** was used to abbreviate the long middle section of the file name. ^a: angle of incidence in degrees, ^b: distance from the lander (x, y) in meters, x represents the eastern direction, y represents the northern direction.

The VNIS on the Yutu rover was designed by Shanghai Institute of Technical Physics, Chinese Academy of Sciences. An Acousto-Optic Tunable Filter (AOTF) was used to split the white light into individual wavelengths to acquire the image and spectrum on the Moon (He et al. 2011). The spatial resolution of SWIR data is around 5 cm (He et al. 2014a). In the VIS/NIR image, SWIR covers a target that corresponds to a circle with a radius of 54 pixels and center at pixel coordinates (96,128) (Fig. 1(b)) (He et al. 2014a).

The detection mode of VIS/NIR images was similar to that of the IIM on Chang'e-1 (He et al. 2011; Liu et al. 2013; He et al. 2014a,b; Liu et al. 2014), MI on SELENE (Ohtake et al. 2010) and M3 on Chandrayaan-1 (Pieters et al. 2009). We use the same method that was applied to data from IIM on Chang'e-1 to reduce the VIS/NIR data from the Yutu rover (Wu et al. 2010). The Level 2B VIS/NIR data were sequentially reduced by bad line (pixel gray-scale slope threshold method), bad point (hot pixel) and flat field corrections (global histogram equalization), and were then converted into reflectance values based on the solar irradiance and angles of incidence (Liu et al. 2013; Liu et al. 2014). The SWIR radiance was directly converted into reflectance based on the solar irradiance and angles of incidence (Liu et al. 2013; Liu et al. 2014).

The VIS/NIR images from Level 2B data, with associated bad line, bad point and flat field corrected cases, are shown in Figure 1. The VIS/NIR images acquired by the Yutu rover have good quality without bad lines (Fig. 1(b)) and rarely show bad points (Fig. 1(c)). Bad point correction ensures that any abnormal pixels in the images are repaired, which will minimize the standard deviation between the samples of the images and ensure good flat field corrections. The composite images of 450 nm (R), 750 nm (G) and 945 nm (B) show that the raw data have a weak heterogeneous response in the horizontal direction (Fig. 2(a)) but this was removed after flat field correction (Fig. 2(b)). The magnitude of the flat field correction for all wavelengths is lower than 2.2%.

3 REFLECTANCE CONVERSION AND SPECTRUM EXTRACTION

Two reflectance conversion methods are usually used in planetary sciences. One relies on a calibration panel to convert the radiance into reflectance (Reid et al. 1999; Liu et al. 2013; Liu et al. 2014). The other employs the solar irradiance to convert the radiance into reflectance (Liu et al. 2013; Ohtake et al. 2010). Liu et al. (2013) discussed the details of converting the radiance into reflectance using the calibration panel. In this work, we just use the solar irradiance for reflectance calibration. In order to compare with the spectra acquired by an orbiting satellite and the spectra of lunar soils determined at the Reflectance Experiment Laboratory facility at Brown University (RELAB), the solar angle of incidence was normalized. The final equation for reflectance calibration is

$$R_j = \frac{\pi I_j}{\cos(i) \int I_0(\lambda) S_j(\lambda) d\lambda}. \quad (1)$$

R_j is the reflectivity at the j^{th} band, I_j is the radiance at the j^{th} band, i is the solar angle of incidence, $I_0(\lambda)$ is the irradiance spectrum of the Sun, cited from Gueymard (2004), and $S_j(\lambda)$ is the spectral response at the j^{th} band.

The average radiance spectra of the four in-situ analyses and solar irradiance spectrum are plotted in Figure 3. The absolute reflectance was calculated based on Equation (1). The VNIS spectrum was extracted from the VIS/NIR image and SWIR spectrum in the overlapping regions. As the detection methods between VIS/NIR and SWIR are different, the reflectance will show a minor gap in the overlapping wavelengths (900–945 nm). Because the SWIR data have smaller spectral jitter than VIS/NIR data, offset correction was applied to shift the VIS/NIR spectra to fit the SWIR spectra (Liu et al. 2014). The offset correction method minimizes the root mean square deviation (Eq. (2)) between the overlapping wavelengths.

$$\text{error} = \sqrt{\sum_{i_\lambda=1}^{10} \left\{ R[\lambda_{\text{VIS/NIR}}(i_\lambda) + \text{offset}] - R[\lambda_{\text{SWIR}}(i_\lambda)] \right\}^2 / N}. \quad (2)$$

In Equation (2), ‘error’ is the root mean square deviation between the overlapping wavelengths of VIS/NIR and SWIR spectra, N is the number of overlapping bands ($N = 10$), i_λ is the i^{th} band of the overlapping wavelengths, $R(\lambda_{\text{VIS/NIR}}(i_\lambda))$ is the reflectivity of VIS/NIR at the i^{th} band, and $R(\lambda_{\text{SWIR}}(i_\lambda))$ is the reflectivity of SWIR at the i^{th} band.

When minimizing the ‘error’ between the reflectance of VIS/NIR and SWIR in the overlapping wavelength range, the best offsets for CD-005~008 are -0.0152 , -0.0029 , 0.0226 and 0.0032 , respectively. The VNIS spectra of CD-005~008 are plotted in Figure 4, showing significant $1 \mu\text{m}$ and $2 \mu\text{m}$ absorption bands, as well as space weathering features, such as a reddened trend and dark reflectance. The VNIS spectra are similar to those of lunar mare soils (15041, Fig. 4) but significantly lower than those of lunar highland soils (67461). Moreover, the spectra of CD-005~008 show significant variation, probably indicating heterogeneous chemical compositions and physical properties (particle size, maturity, roughness, etc.) on small scales (Fig. 4).

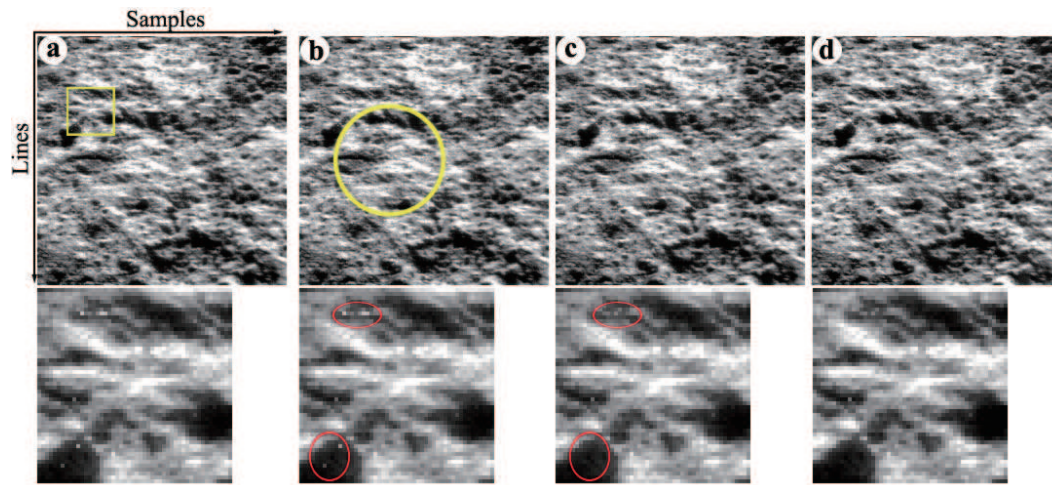


Fig. 1 Gray VIS/NIR images of (a) CD-005 representing raw data, (b) bad line corrected, (c) bad point corrected and (d) flat field corrected cases. The corresponding lower images are the magnified local regions outlined by a square in (a). CD-005 has no bad lines. Bad point correction has removed the abnormal pixels in the images. The region outlined by a circle in (b) is the SWIR detection target.

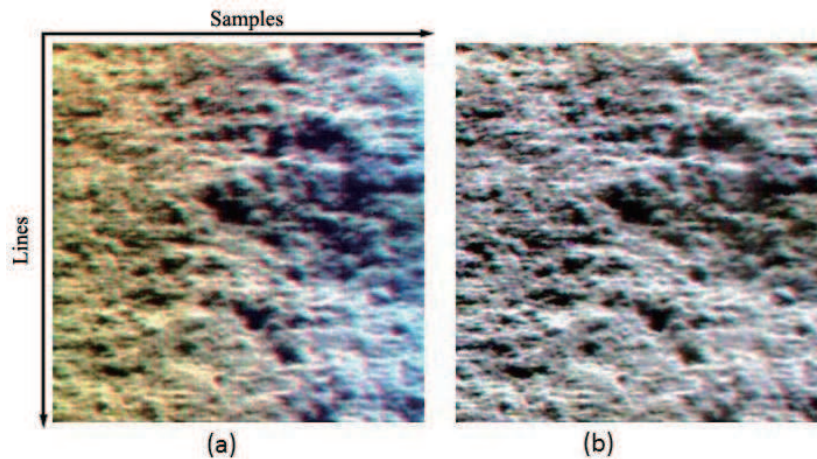


Fig. 2 Composite images (R: 450 nm, G: 750 nm, B: 945 nm) of raw data (a) and flat field corrected (b) cases. The raw data show a heterogeneous response with yellow on the left side and blue on the right side. In contrast, the image after flat field correction shows a homogeneous response. Image ID is CD-008.

4 SHADOW EFFECT

As shown in Figure 1, the VIS/NIR images show significant dark regions with similar stretching directions. The local dark regions are the shadows constrained by the in-situ observation angles. The presence of shadows will have a strong effect on the average reflectance of entire images. We assess the shadow effects in the VIS/NIR-SWIR overlapping regions and entire images.

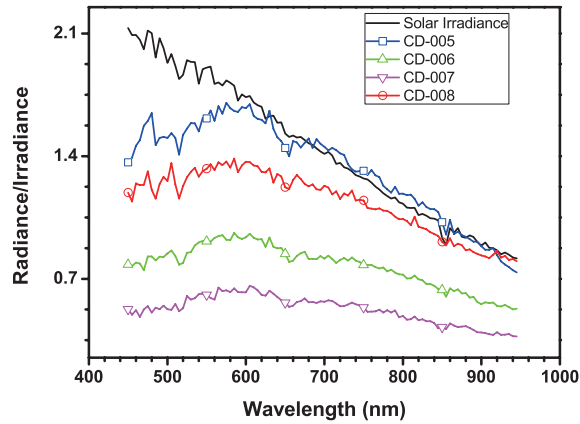


Fig. 3 Radiance spectra of CD-005~008 and a solar irradiance spectrum are plotted for comparison. Radiance is in $\mu\text{W cm}^{-2} \text{nm}^{-1} \text{sr}^{-1}$ and irradiance is in $10^2 \mu\text{W cm}^{-2} \text{nm}^{-1}$ cited from Gueymard 2004.

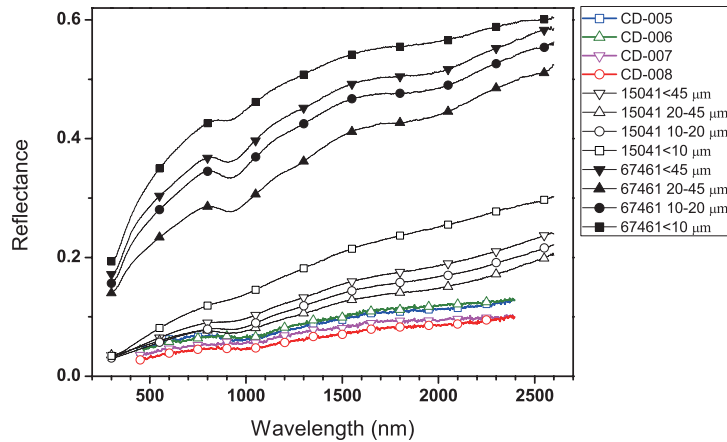


Fig. 4 The VNIS spectra of CD-005~008. The spectra of Apollo 15 soils (15041, lunar mare soils) and Apollo 16 soils (67461, lunar highland soils), from Pieters et al. 2000, with different grain sizes are also plotted for comparison.

In order to assess the shadow effect, R_{750} (reflectance at 750 nm) was used to classify an entire image into shadow regions and illuminated regions. In order to determine the threshold of the shadows, CD-007 was used as an example because it showed large shadow areas (Fig. 5(b)). Reflectance at 750 nm (R_{750}) of CD-007 shows two overlapping peaks in the reflectance range 0.017–0.05 with a local minimum around 0.03 (Fig. 5(a)), which was used as the input of the shadow threshold. We can modify the threshold around the input value to find the best match of the shadow regions determined from the threshold (value pointed out by an arrow in Fig. 5(a)) and from the corresponding gray image (Fig. 5(b)). From the reflectance gray image of CD-007 (Fig. 5(b)), the dark areas represent shadow regions rather than an assemblage of finer dust because they share a similar stretch in the light direction (indicated by an arrow in Fig. 5(b)). Furthermore, the finer dust particles of

lunar soils usually have higher reflectance compared with that of coarser grains as shown in Figure 4 (reflectance of 15041 at $<10\ \mu\text{m}$ is significantly higher than that of 15041 at $20\text{--}45\ \mu\text{m}$). Finally, the shadow thresholds of R_{750} in CD-005~008 are 0.042, 0.032, 0.025 and 0.03, respectively. The average reflectance ($R(\lambda)$) of the overlapping regions is lower than the reflectance ($R_{\text{illuminated}}(\lambda)$) in the area that excludes the shadow pixels. The shadow effect also exists in the SWIR ranges, although recorded as a spectrum. Based on the assessment with VIS/NIR ranges, the reflectance enhancement can be calculated by Equation (3)

$$k = \frac{1}{N} \sum_{i_{\lambda}=1}^{100} \frac{R_{\text{illuminated}}(\lambda)}{R(\lambda)}, \quad (3)$$

where k is the shadow correction coefficient, i_{λ} is the i^{th} band of the VIS/NIR wavelengths, λ is the wavelength in nm with an interval of 5 nm, $R_{\text{illuminated}}(\lambda)$ is average reflectivity at λ when excluding the shadow pixels, $R(\lambda)$ is the average reflectivity at λ of all the overlapping regions, and N represents the number of bands included in the calculation ($N=100$ for VIS/NIR).

The calculated shadow correction coefficients (k) of CD-005~008 are 1.08, 1.12, 1.17 and 1.12, respectively. The same k that was used for VIS/NIR was also used to correct the corresponding SWIR reflectance. The jump in reflectance between VIS/NIR and SWIR was corrected by Equation (2). The offsets of CD-005~008 were 0.0003, 0.0166, 0.0177 and -0.002 , respectively. The VNIS spectra after shadow correction showed a higher reflectance compared to the uncorrected spectra (Fig. 6).

For the entire VIS/NIR images, the shadow regions of CD-005~008 are 14%, 20%, 30% and 12%, respectively, based on the reflectance shadow thresholds at 750 nm. The shadow corrected results are plotted in Figure 7. The reflectance enhancements after shadow correction are 8%, 13%, 24% and 7% for CD-005~008, respectively. The reflectance enhancements are positively correlated with the shadow areas, indicating that the shadow effect cannot be ignored.

5 IMPACT OF THE SHADOW EFFECT ON FEO CONTENT INVERSION

Because the VIS/NIR data are recorded as images, there are two ways to calculate the FeO contents. One is to use the image to calculate FeO contents and its distribution. The other regards the entire/partial image as spectra, like SWIR, to calculate the FeO contents.

In order to estimate the impact of the shadow effect on chemical composition inversion, FeO content of CD-005, which was calculated based on the algorithm used by Lucey's method (Lucey et al. 2000), is shown in Figure 8(a). Θ_{Fe} is defined by Equation (4) and FeO content is calculated using Equation (5) from (Lucey et al. 2000).

$$\Theta_{\text{Fe}} = -a \tan \left[\frac{R_{950}/R_{750} - 1.23}{R_{750} - 0.04} \right]. \quad (4)$$

R_{950} and R_{750} are the reflectivity at 950 nm and 750 nm of the VNIS spectra, respectively.

$$\text{FeO} = 17.427 \times \Theta_{\text{Fe}} - 7.565. \quad (5)$$

The FeO contents of CD-008 can be classified into two endmembers (shadow regions and illuminated regions). The FeO contents of the shadow regions are set to be 0 wt.% because their relatively dark reflectance will produce a negative denominator ($R_{750} - 0.04$) for Θ_{Fe} . The illuminated regions show relatively homogeneous FeO contents (18.3 ± 0.9 wt.%, 1 standard deviation (SD)), varying from 15 wt.% to 19.8 wt.% with a peak around 18.1 wt.% (Fig. 8(b)). If including the shadow regions, then the average FeO content of CD-005 is 16.1 ± 6.0 wt.% (1SD), 2.2 wt.% lower than that of the illuminated regions. Processed in the same way as CD-005, the average FeO contents of the illuminated regions in CD-006~008 are 17.3 ± 2.4 wt.%, 17.9 ± 2.3 wt.% and

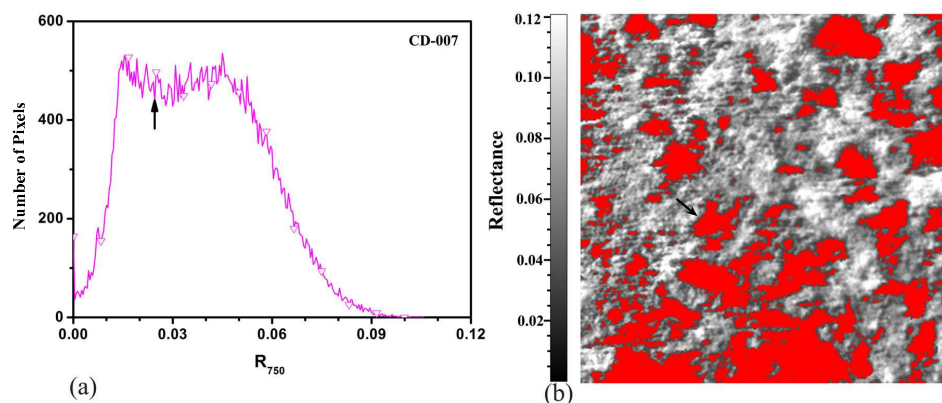


Fig. 5 (a) Histogram of R_{750} in CD-007. The value pointed out by an arrow was finally used for classifying the image into shadow and illuminated regions. (b) The corresponding image can be classified as shadow regions (*red areas*) and illuminated regions (*gray areas*).

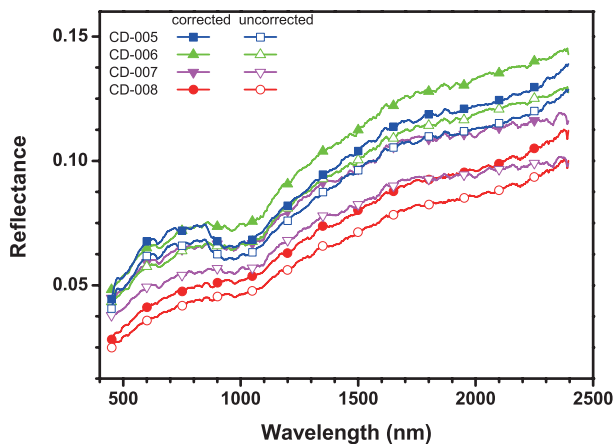


Fig. 6 Shadow corrected and uncorrected spectra of CD-005~008 in the overlapping regions between VIS/NIR and SWIR.

17.4 ± 2.4 wt.%, respectively. If including the shadow regions, the average FeO contents of CD-006~008 are 13.3 ± 7.6 wt.%, 13.0 ± 8.2 wt.% and 13.2 ± 7.7 wt.%, which are 4.0 wt.%, 4.9 wt.% and 4.2 wt.% lower than those of the illuminated regions, respectively.

Alternatively, the FeO contents can be derived from the VIS/NIR spectra. In this study, the VIS/NIR-SWIR overlapping region was chosen to discuss the effects of shadow and offset corrections for calculating the FeO contents. Lucey's method (Lucey et al. 2000) was used to calculate FeO contents and the results are listed in Table 2. Before shadow correction, the FeO contents of CD-005~008 varied from 18.3–18.8 wt.%, except for CD-007, which showed a negative result caused by extremely low reflectivity at 750 nm (Table 2). After shadow correction, the FeO contents of CD-005~008 varied from 17.9–18.0 wt.%, which was comparable with that before shadow corrections except for CD-007 (Table 2). The shadow corrected spectra usually have higher reflectivity, which results in lower Θ_{Fe} and lower FeO contents compared with those of the uncorrected

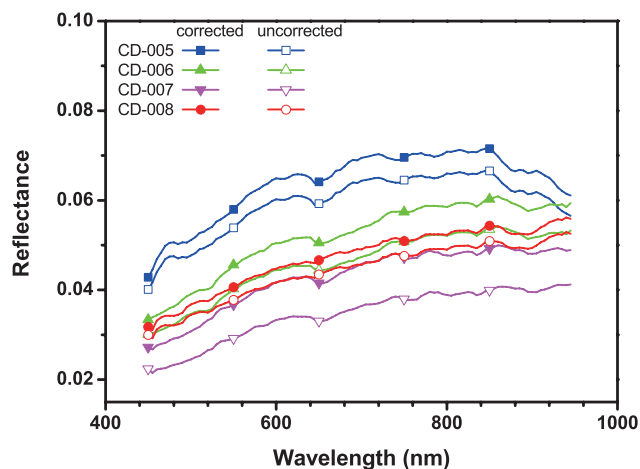


Fig. 7 The shadow corrected and uncorrected VIS/NIR spectra of CD-005~008.

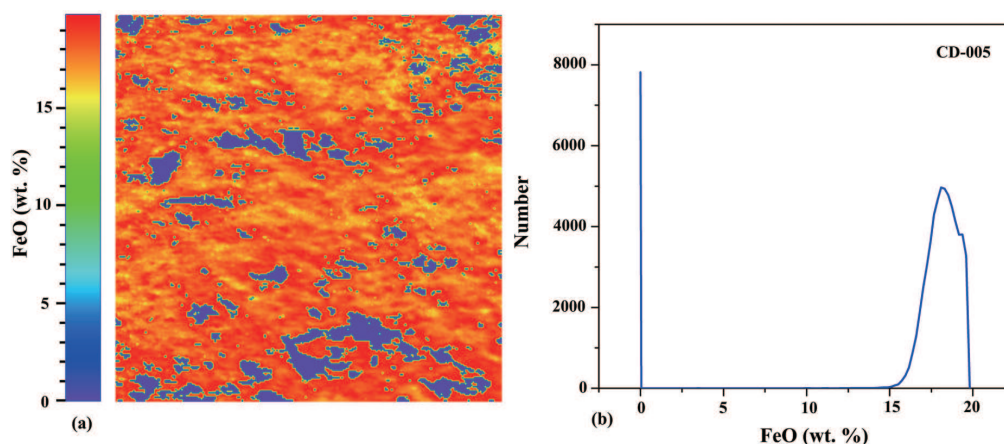


Fig. 8 (a) FeO content distribution of CD-005 using Lucey's method (Lucey et al. 2000). (b) Histogram of FeO content in CD-005.

shadow case (Table 2). When excluding the darkest reflectance of CD-007, the FeO contents after shadow correction are more homogeneous (18.0 ± 0.04 wt.%) compared with that (18.6 ± 0.27 wt.%) of the uncorrected shadow case (Table 2). At last, VNIS spectra were calculated by shifting the VIS/NIR spectra to fit SWIR spectra with corresponding offsets. The FeO contents of CD-005~008 from VNIS spectra (Fig. 6) varied from 16.2–18.3 wt.% (Table 2). The FeO contents are sensitive to the offsets, e.g., the FeO contents of CD-006 and CD-007 after offset corrections are 1.7 wt.% and 1.8 wt.% lower than those of the shadow corrected cases, respectively (Table 2), suggesting that shifting VIS/NIR to fit SWIR with large offsets would not be suitable for FeO calculation.

The shadow corrected FeO contents calculated from VIS/NIR images are consistent with those from VIS/NIR spectra within statistical uncertainties. However, the shadow uncorrected FeO contents (13.0–16.1 wt.%) calculated from VIS/NIR images are much lower than those (18.3–18.8 wt.%) from VIS/NIR spectra, probably diluted by the shadows without FeO contents. These results suggest

Table 2 FeO contents of CD-005~008 using Lucey's method (Lucey et al. 2000) from shadow uncorrected, shadow corrected and shadow+offset corrected VIS/NIR spectra in the VIS/NIR-SWIR overlapping region.

Name	R_{750} (nm)	R_{945} (nm)	Θ_{Fe}	FeO (wt.%)
Before shadow correction				
CD-005	0.0666	0.0586	1.4852	18.3
CD-006	0.0490	0.0523	1.4981	18.5
CD-007	0.0398	0.0421	-1.5690	-34.9
CD-008	0.0450	0.0495	1.5156	18.8
Average*				18.6±0.27
After shadow correction				
CD-005	0.0718	0.0632	1.4684	18.0
CD-006	0.0549	0.0577	1.4640	17.9
CD-007	0.0468	0.0481	1.5288	19.1
CD-008	0.0505	0.0550	1.4680	18.0
Average				18.3±0.54
After shadow and offset corrections				
CD-005	0.0748	0.0662	1.4571	17.8
CD-006	0.0715	0.0743	1.3648	16.2
CD-007	0.0645	0.0658	1.4274	17.3
CD-008	0.0485	0.0530	1.4844	18.3
Average				17.4±0.89

Notes: * Average FeO contents excluding CD-007. R is the reflectivity at 750 nm and 945 nm of the VNIS spectra. The column FeO lists the FeO contents determined using the different corrections.

that the shadow effect must be corrected before calculating the FeO contents. The correction for the shadow effect will increase the derived FeO contents by up to 0.6 wt.% for VIS/NIR spectra and decrease the derived FeO contents by up to 2.2–4.9 wt.% for VIS/NIR images. The FeO contents of CD-005~008 after shadow correction are around 18.0 wt.%, which is significantly higher than lunar highland soils (Taylor et al. 2001). The shadow effects are not large enough to misclassify lunar mare soil as highland soil.

6 CONCLUSIONS

The Level 2B data were processed and converted to reflectance. The VNIS spectra were calculated by shifting the VIS/NIR to fit SWIR spectra. The VNIS spectra of Chang'e-3 show typical spectra of lunar mare soils, with significant space weathering features. The shadow effect was observed in the VIS/NIR images. The correction for the shadow effect will increase reflectance by up to 17% for the local regions and by 24% for the entire images, and affect the results related to calculations of FeO contents. For VIS/NIR images, the correction for the shadow effect will decrease the derived FeO contents by up to 4.9 wt.%. For VIS/NIR spectra in the VIS/NIR-SWIR overlapping region, the correction for the shadow effect will increase the derived FeO contents by up to 0.6 wt.%. The large offsets when shifting the VIS/NIR to fit SWIR spectra will significantly decrease the derived FeO contents by up to 1.8 wt.%. Finally, we estimate the FeO contents of CD-005~008 after shadow corrections to around 18.0 wt.%.

Acknowledgements The constructive reviews by two anonymous referees and suggestions of the RAA editorial staff significantly improved this paper. The Level 2B data were provided by the Ground Segment for Data, Science and Application (GSDSA) of China's Lunar Exploration Program. This study was supported by the Chinese Academy of Sciences (KGZD-EW-603) and the National Natural Science Foundation of China (Grant No. 41103031).

References

- Gillis, J. J., Jolliff, B. L., & Elphic, R. C. 2003, *Journal of Geophysical Research (Planets)*, 108, 5009
- Gueymard, C. A. 2004, *Solar Energy*, 76, 423
- He, Z., Shu, R., & Wang, J. 2011, in *International Symposium on Photoelectronic Detection and Imaging 2011*, 8196, 819625
- He, Z. P., Wang, B. Y., Lv, G., et al. 2014a, *Review of Scientific Instruments*, 85, 083104
- He, Z.-P., Wang, B.-Y., Lü, G., et al. 2014b, *RAA (Research in Astronomy and Astrophysics)*, 14, 1567
- Helfenstein, P., & Shepard, M. K. 1999, *Icarus*, 141, 107
- Liu, B., Liu, J.-Z., Zhang, G.-L., et al. 2013, *RAA (Research in Astronomy and Astrophysics)*, 13, 862
- Liu, B., Li, C.-L., Zhang, G.-L., et al. 2014, *RAA (Research in Astronomy and Astrophysics)*, 14, 1578
- Lucey, P. G., Blewett, D. T., & Jolliff, B. L. 2000, *J. Geophys. Res.*, 105, 20297
- Ohtake, M., Matsunaga, T., Yokota, Y., et al. 2010, *Space Sci. Rev.*, 154, 57
- Ohtake, M., Takeda, H., Matsunaga, T., et al. 2012, *Nature Geoscience*, 5, 384
- Pieters, C. M., Taylor, L. A., Noble, S. K., et al. 2000, *Meteoritics and Planetary Science Supplement*, 35, 127
- Pieters, C. M., Goswami, J. N., Clark, R. N., et al. 2009, *Science*, 326, 568
- Reid, R. J., Rueffer, P., Gliem, F., et al. 1999, *J. Geophys. Res.*, 104, 8907
- Shkuratov, Y., Kaydash, V., Korokhin, V., et al. 2011, *Planet. Space Sci.*, 59, 1326
- Shultz, P. H., & Spudis, P. D. 1983, *Nature*, 302, 233
- Taylor, L. A., Pieters, C. M., Keller, L. P., Morris, R. V., & McKay, D. S. 2001, *J. Geophys. Res.*, 106, 27985
- Wu, Y., Xue, B., Zhao, B., et al. 2012, *Journal of Geophysical Research (Planets)*, 117, 2001
- Wu, Y., Zhang, X., Yan, B., et al. 2010, *Science China Physics, Mechanics, and Astronomy*, 53, 2160